



The Evolution of Molecular Gas Fraction Traced by the CO Tully–Fisher Relation

Jacob W. Isbell^{1,2} , Rui Xue¹ , and Hai Fu¹ ¹ Department of Physics & Astronomy, The University of Iowa, 203 Van Allen Hall, Iowa City, IA 52242, USA² Max-Planck-Institut für Astronomie, Königstuhl 17, Heidelberg D-69117, Germany

Received 2018 November 6; revised 2018 December 3; accepted 2018 December 13; published 2018 December 20

Abstract

Carbon monoxide (CO) observations show a luminosity–line width correlation that evolves with redshift. We present a method to use CO measurements alone to infer the molecular gas fraction (f_{mol}) and constrain the CO–H₂ conversion factor (α_{CO}). We compile from the literature spatially integrated low- J CO observations of six galaxy populations, including a total of 449 galaxies between $0.01 \leq z \leq 3.26$. The CO data of each population provide an estimate of the α_{CO} -normalized mean molecular gas fraction ($f_{\text{mol}}/\alpha_{\text{CO}}$). The redshift evolution of the luminosity–line width correlation thus indicates an evolution of $f_{\text{mol}}/\alpha_{\text{CO}}$. We use a Bayesian-based Monte Carlo Markov Chain sampler to derive the posterior probability distribution functions of $f_{\text{mol}}/\alpha_{\text{CO}}$ for these galaxy populations, accounting for random inclination angles and measurement errors in the likelihood function. We find that the molecular gas fraction evolves rapidly with redshift, $f_{\text{mol}} \propto (1+z)^\beta$ with $\beta \simeq 2$, for both normal star-forming and starburst galaxies. Furthermore, the evolution trend agrees well with that inferred from the Kennicutt–Schmidt relation and the star-forming main sequence. Finally, at $z < 0.1$ normal star-forming galaxies (SFGs) require a $\sim 5\times$ larger α_{CO} than starburst galaxies to match their molecular gas fractions, but at $z > 1$ both star-forming types exhibit sub-Galactic α_{CO} values and normal SFGs appear more gas rich than starbursts. Future applications of this method include calibrating Tully–Fisher relations without inclination correction and inferring the evolution of the atomic gas fraction with HI observations.

Key words: galaxies: evolution – galaxies: ISM – galaxies: star formation

1. Introduction

In the Milky Way, star formation occurs in giant molecular clouds (GMCs; e.g., McKee & Ostriker 2007), which are cold, dense, and self-gravitating structures with a typical spatial extent of ~ 50 pc (e.g., Blitz 1993). As the apparent fuel of star formation, molecular gas plays a key role in galaxy evolution (e.g., Kennicutt & Evans 2012). Even though the sub-pc-scale physics of star formation is still not well understood, empirically the star formation rate (SFR) surface density is found to tightly correlate with the molecular gas mass (M_{mol}) surface density on kpc scales, following the Kennicutt–Schmidt relation (e.g., Wong & Blitz 2002; Bigiel et al. 2008). As a result, the fraction of molecular gas within a galaxy’s total baryonic mass ($f_{\text{mol}} \equiv M_{\text{mol}}/M_{\text{bary}}$) determines its specific SFR (sSFR = SFR/ M_*). In fact, the redshift evolution of the star-forming main sequence (SFR $\propto M_*$; e.g., Noeske et al. 2007) is interpreted as the evolution of the molecular gas fraction (e.g., Bouché et al. 2010). Being able to measure f_{mol} directly as a function of redshift is thus crucial for our understanding of the evolution of star-forming galaxies (SFGs).

The brightest molecular lines from galaxies are emitted by carbon monoxide ($^{12}\text{C}^{16}\text{O}$, hereafter CO) because it is the second most abundant molecule and its low-level rotational transitions are easily excitable in GMC-like environments. Therefore, many previous studies of the molecular gas content of galaxies have used the CO line luminosity to estimate the total molecular gas mass, assuming that the two are related by a CO–H₂ conversion factor (see Bolatto et al. 2013, for a review). Combined with stellar mass estimates from stellar population synthesis modeling of the optical-to-infrared (IR) spectral energy distributions (SEDs), the molecular gas fraction can be estimated for individual galaxies at significant redshifts (e.g., Tacconi et al. 2018), where the atomic/ionized gas

contribution is likely negligible due to higher molecular-to-atomic gas ratios (e.g., Obreschkow & Rawlings 2009; Lagos et al. 2011). Using this approach, f_{mol} is found to increase with redshift and correlate with sSFR—albeit with large scatters (e.g., Tacconi et al. 2010, 2013)—as is expected from the Kennicutt–Schmidt relation. However, stellar mass estimates from population synthesis models are known to suffer from a number of systematic degeneracies. In particular, different assumed star formation histories alone can lead to stellar mass estimates that differ by almost an order of magnitude (e.g., Michałowski et al. 2012). To avoid such uncertainties, here we propose to estimate the molecular gas fraction using the Tully–Fisher relation.

The original Tully–Fisher relation (TFR; Tully & Fisher 1977) is an empirical correlation between the B -band absolute magnitude and the HI 21 cm line width of local disk galaxies. In the past four decades, multiple flavors of the TFR have been established by using luminosities at longer wavelengths (e.g., Tully & Courtois 2012; Sorce et al. 2013; Tiley et al. 2016) and/or by adopting kinematics traced by other emission lines, e.g., [O II] $\lambda 3776$ (Chiu et al. 2007) and CO (Schoniger & Sofue 1994; Ho 2007; Davis et al. 2011). In addition, the relation is also expanded to samples at significant redshifts (e.g., Chiu et al. 2007; Cresci et al. 2009; Turner et al. 2017; Übler et al. 2017). Given the almost constant mass-to-light ratio in rest-frame near-IR wavelengths, luminosity-based TFR can be converted to mass-based TFRs (McGaugh 2012; Zaritsky et al. 2014; Tiley et al. 2016; Topal et al. 2018), providing a method to estimate galaxy masses from simply a line profile.

Here we present a method to measure the evolution of molecular gas fraction in massive galaxies between $0 < z < 3$ using the CO TFR. This Letter is organized as follows: in Section 2 we describe the compilation of galaxy-integrated CO

line widths and luminosities, in Section 3 we introduce the Bayesian-based statistical method to infer the molecular gas fraction from CO data and the TFR, and in Section 4 we present our results and discuss the systematic uncertainties. We close with a summary and discuss future applications of this method in Section 5. Throughout we adopt the Λ CDM cosmology with $\Omega_m = 0.3$, $\Omega_\Lambda = 0.7$, and $H_0 = 70 \text{ km s}^{-1} \text{ Mpc}^{-1}$.

2. Data Compilation

We have compiled spatially integrated low- J ($J_{\text{up}} \leq 3$) CO measurements of 449 galaxies between $0.01 < z < 3.26$ from the literature. Low- J transitions are preferred over high- J transitions because they have: (1) less extreme excitation conditions, (2) lower scatter in the CO spectral line energy distribution (e.g., Greve et al. 2014), and (3) more spatially extended distribution (e.g., Ivison et al. 2011; Saito et al. 2017). To carry out our analysis in Section 3, we only need three observables—the redshift, the line flux, and the line width.

The redshift and the line flux coupled with a cosmology give the CO line luminosity (L'_{CO}), which is normally defined as the velocity-area-integrated CO brightness temperature (Solomon et al. 1997):

$$L'_{\text{CO}} = 3.25 \times 10^7 S_{\text{CO}} \Delta V \nu_{\text{obs}}^{-2} D_L^2 (1+z)^{-3} \quad (1)$$

where $S_{\text{CO}} \Delta V$ is the integrated line flux in Jy km s^{-1} , ν_{obs} is the observed frequency in GHz, D_L is the luminosity distance in Mpc. The resulting L'_{CO} is in units of $L_l \equiv \text{K km s}^{-1} \text{ pc}^2$. To homogenize the different cosmologies adopted in the various references, we have converted the reported L'_{CO} to our adopted cosmology. Additionally, we convert L'_{CO} from higher J transitions to the equivalent CO(1 \rightarrow 0) luminosity using the observed mean correction factor: $R_{J1} \equiv L'_{\text{CO}, J \rightarrow J-1} / L'_{\text{CO}, 1 \rightarrow 0}$. For (ultra-)luminous infrared galaxies (ULIRGs) and submillimeter-bright galaxies (SMGs), we adopt the mean SMG values of $R_{21} = 0.85$ and $R_{31} = 0.66$; and for the normal SFGs, we adopt $R_{21} = 0.9$ and $R_{31} = 0.6$, which are the mean values from high-redshift color-selected SFGs (see Table 2 in Carilli & Walter 2013).

We adopt the FWHM (hereafter w in km s^{-1}) values reported in each reference to characterize CO line widths. The spectral resolutions are generally much smaller than the line widths, so instrumental broadening has a negligible effect. We note that these surveys measure w in various ways, and the values were often estimated from best-fit parametrized models to the actual spectra. However, as shown by previous studies (e.g., Bothwell et al. 2013; Magdis et al. 2014; Tiley et al. 2016), there are no systematic offsets among the w -values derived from different techniques, because the parameterized models must represent the observed line profiles reasonably well.

The compiled references are listed in Table 1. We have grouped them into six populations based on their redshift range and source selection criteria. Our compilation is not intended to be complete; instead, we have selected the references that include relatively large numbers of objects ($N \geq 8$) in their corresponding category to minimize inhomogeneity in the data set. There are three populations of normal SFGs and three populations of starburst galaxies.

1. *Local SFGs*: We include CO(1 \rightarrow 0) detections of 214 galaxies between $0.025 < z < 0.05$ from the CO Legacy Database for the GALEX Arecibo Sloan Digital Sky Survey (SDSS) Survey (COLD GASS; Saintonge et al. 2011, 2017). This survey used the Institut de Radio-astronomie Millimétrique (IRAM) 30 m telescope and targeted 366 stellar-mass-selected galaxies with $10^{10} M_\odot < M_* < 10^{11.5} M_\odot$. We deliberately exclude the 166 galaxies in the COLD GASS-low sample ($M_* < 10^{10} M_\odot$ and $z < 0.02$), because these galaxies are not massive enough to be comparable with the samples at higher redshifts. The CO line widths were measured using the method of Springob et al. (2005), which fits a linear slope to each side of the line profile and takes the width at half maximum of these fits.
2. *Local (U)LIRGs*: We include CO(1 \rightarrow 0) detections of 68 galaxies in 56 (U)LIRGs with $L_{\text{IR}} > 10^{11} L_\odot$ between $0.01 < z < 0.09$ from Yamashita et al. (2017). The reported CO line widths were measured directly from the emission profiles. These galaxies were observed using the Nobeyama Radio Observatory (NRO) 45 m telescope and were selected from the Great Observatories All-sky LIRG Survey (GOALS; Armus et al. 2009).
3. *Intermediate-redshift SFGs*: We include 49 CO(1 \rightarrow 0) Atacama Large Millimeter/submillimeter Array (ALMA) detections of galaxies between $0.03 < z < 0.33$ from Villanueva et al. (2017). The galaxies were selected from the *Herschel*-ATLAS survey to have $> 3\sigma$ detections in both the $160 \mu\text{m}$ and $250 \mu\text{m}$ bands. The reported line widths are measured from best-fit single-Gaussian profiles.
4. *Intermediate-redshift ULIRGs*: We include IRAM 30 m CO detections of 28 galaxies between $0.61 < z < 0.91$ from Combes et al. (2011, 2013) and 8 galaxies between $0.22 < z < 0.44$ from Magdis et al. (2014). The galaxies in Combes et al. (2011, 2013) and Magdis et al. (2014) are ULIRGs with $L_{\text{IR}} > 10^{12.45} L_\odot$ and detected at $60 \mu\text{m}$ (*IRAS*) and $250 \mu\text{m}$ (*Herschel*-SPIRE) respectively. Both samples obtain w from the best-fit single-Gaussian models to the line profiles.
5. *High-redshift SFGs*: We include CO(3 \rightarrow 2) detections of 51 main-sequence galaxies between $1.00 < z < 2.43$ from the Plateau de Bure High- z Blue Sequence Survey (PHIBBS; Tacconi et al. 2013). These galaxies have $M_* > 2.5 \times 10^{10} M_\odot$ and $\text{SFR} > 30 M_\odot \text{ yr}^{-1}$. The authors report the characteristic circular velocity (v_c) estimated from either the line FWHM for unresolved sources or the inclination-angle-corrected velocity gradient for resolved sources. Because the line FWHMs, the velocity gradients, and the inclination angles are not listed in their tables, we use the isotropic virial estimate adopted by the authors for all their galaxies to convert v_c to w : $w/v_c = \sqrt{(8 \ln 2)/3} = 1.36$.
6. *High-redshift SMGs*: We include 19 CO detections of SMGs ($S_{850} > 1 \text{ mJy}$) between $1.19 < z < 3.10$ from Bothwell et al. (2013). Line widths are from the intensity-weighted second moment of each CO spectrum, converted to the equivalent Gaussian w . The authors argue that this method is better for low signal-to-noise spectra, where Gaussian fits may fail to achieve sensible results. We also include CO(1 \rightarrow 0) detections of 12 *Herschel*-selected bright SMGs using the 100-m Green Bank

Table 1
Compilation of CO Measurements and Best-fit Model Parameters

References ^a	Telescope	Redshift Range	N Sources ^b	CO J_{up}	$\log f'_{\text{mol}} \text{ }^{\text{c}}$ $\log(L_I M_{\odot}^{-1})$	$\sigma \text{ }^{\text{d}}$ (dex)	$f_{\text{mol}} \text{ }^{\text{e}}$
Local Star-forming Galaxies							
Saintonge et al. (2017)	IRAM 30 m	0.03–0.05	214	1	$-1.85_{-0.04}^{+0.05}$	$0.46_{-0.04}^{+0.04}$	$1.4_{-0.2}^{+0.1}\%$
Local ULIRG							
Yamashita et al. (2017)	NRO 45 m	0.01–0.09	68	1	$-1.18_{-0.10}^{+0.10}$	$0.62_{-0.07}^{+0.08}$	$6.7_{-1.7}^{+1.3}\%$
Intermediate-redshift Star-forming Galaxies							
Villanueva et al. (2017)	ALMA	0.03–0.33	49	1	$-0.90_{-0.09}^{+0.09}$	$0.48_{-0.07}^{+0.08}$	$12.6_{-2.4}^{+2.9}\%$
Intermediate-redshift ULIRGs							
Combes et al. (2011, 2013)	IRAM 30 m	0.61–0.91	28	2,3	$-0.52_{-0.12}^{+0.12}$	$0.60_{-0.08}^{+0.10}$	$30.3_{-9.7}^{+7.4}\%$
Magdis et al. (2014)	IRAM 30 m	0.22–0.44	8	1,2,3			
High-redshift Star-forming Galaxies							
Tacconi et al. (2013)	PdBI	1.00–2.43	51	3	$-0.36_{-0.10}^{+0.11}$	$0.57_{-0.08}^{+0.09}$	$44.1_{-12.2}^{+9.4}\%$
High-redshift Submillimeter Galaxies							
Bothwell et al. (2013)	PdBI	1.19–3.26	31	1,2,3	$-0.54_{-0.09}^{+0.09}$	$0.36_{-0.06}^{+0.08}$	$28.7_{-6.7}^{+5.4}\%$
Harris et al. (2012)	GBT 100 m	2.19–3.26	12	1			

Notes.

^a The six galaxy populations in our study are highlighted in bold font, followed by the included references.

^b Bold face values indicate the total number of sources in each population.

^c The best-fit α_{CO} -normalized molecular gas fraction $\log f'_{\text{mol}} = \log(f_{\text{mol}}/\alpha_{\text{CO}})$ (see Section 3).

^d The best-fit dispersion parameter σ in dex, which captures the observational errors and the intrinsic scatter in the baryonic TFR (see Sections 3 and 4.2).

^e The molecular gas fraction calculated from $\log f'_{\text{mol}}$ assuming a CO–H₂ conversion factor of $\alpha_{\text{CO}} = 1.0 M_{\odot}/L_I$.

Telescope (GBT) between $2.19 < z < 3.26$ from Harris et al. (2012). The reported line widths come from the best-fitted single-Gaussian profiles. Because these *Herschel* galaxies are gravitationally lensed, we correct the observed L'_{CO} using the magnification factors from the lens models of Bussmann et al. (2013).

We present all of the CO measurements in Figure 1. The various populations show a similar distribution in line width with a median around 300 km s^{-1} , except the SMGs, which show a ~ 0.2 dex offset to higher velocities. On the other hand, the line luminosities increase with redshift, as expected from the limited instrument sensitivity. Even without correcting the line widths for the inclination angles, the correlation between L'_{CO} and w is evident within each galaxy population. This is expected from the TFR if the galaxies in each population have similar molecular gas fraction ($f_{\text{mol}} \equiv M_{\text{mol}}/M_{\text{bary}}$) and CO–H₂ conversion factor ($\alpha_{\text{CO}} \equiv M_{\text{mol}}/L'_{\text{CO}}$). The dashed lines in Figure 1 show the expected correlations at a range of fixed $f_{\text{mol}}/\alpha_{\text{CO}}$ ratios, and they seem to fit the data points well if we allow $f_{\text{mol}}/\alpha_{\text{CO}}$ to vary among populations. This hints at an evolution that we will explore in detail in the next sections.

3. Analysis Method

The CO line luminosity L'_{CO} traces the molecular gas mass M_{mol} through the CO–H₂ conversion factor, while the inclination-corrected line width ($W \equiv w/\sin i$ where $i = 0$ is face-on) provides a measure of the baryonic mass M_{bary} through the TFR. Therefore, each CO measurement pair of L'_{CO} and W offers an estimate of the ratio between the molecular gas fraction (f_{mol}) and the CO–H₂ conversion factor (α_{CO}):

$$\frac{L'_{\text{CO}}}{M_{\text{bary}}} = \frac{L'_{\text{CO}} M_{\text{mol}}}{M_{\text{mol}} M_{\text{bary}}} = \frac{f_{\text{mol}}}{\alpha_{\text{CO}}} \equiv f'_{\text{mol}} \quad (2)$$

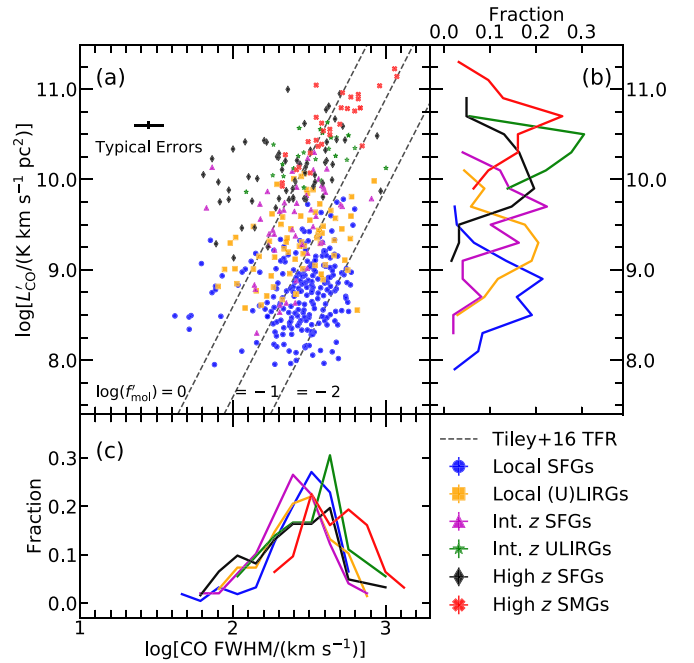


Figure 1. Compiled CO measurements of the six galaxy populations in Table 1. (a) CO luminosity (L'_{CO}) vs. line FWHM (w). Data points are color-coded by their population, as described by the legend. Typical errors are 25% (0.11 dex) in w and 15% (0.07 dex) in L'_{CO} . The dashed lines show a range of $f'_{\text{mol}} \equiv f_{\text{mol}}/\alpha_{\text{CO}}$ values used to convert line width-inferred masses to L'_{CO} (refer to Equations (2) and (3)). (b) Distributions in line luminosity, plotted in units of fraction per dex for 0.2 dex bins. (c) Distributions in line width, plotted in units of fraction per dex for 0.12 dex bins.

For simplicity, we have defined the above ratio as f'_{mol} , the α_{CO} -normalized molecular gas fraction. Our goal is to measure the average f'_{mol} values of different galaxy populations as a

function of redshift, from only a pair of CO-based observables. The detailed procedures are described below.

To estimate M_{bary} , we adopt the CO baryonic TFR in the form of

$$\log\left(\frac{M_{\text{bary}}}{M_{\odot}}\right) = a + b\left[\log\left(\frac{W}{\text{km s}}\right) - c\right], \quad (3)$$

where W is the inclination-corrected CO line width, i.e., $W = w/\sin i$. For comparison, the CO *stellar-mass* TFR derived by Tiley et al. (2016) is

$$\log\left(\frac{M_{\star}}{M_{\odot}}\right) = 10.51 \pm 0.04 + (3.3 \pm 0.3)\left[\log\left(\frac{W}{\text{km s}}\right) - 2.58\right], \quad (4)$$

which is calibrated using a large sample of local SFGs from COLD GASS (Saintonge et al. 2011, 2017). By incorporating the atomic gas mass from GASS (Catinella et al. 2018) and the Arcicibo Legacy Fast ALFA (ALFALFA; Haynes et al. 2018), and the stellar mass and the molecular gas mass from COLD GASS, we can estimate the average stellar mass fraction, $f_{\star} \equiv M_{\star}/M_{\text{bary}} = M_{\star}/(M_{\star} + M_{\text{H I}} + M_{\text{mol}})$, for the COLD GASS galaxies. As expected, these galaxies are dominated by stellar mass with $\langle f_{\star} \rangle \simeq 80\%$, which indicates that this *stellar-mass* TFR is a good approximation of the local *baryonic* TFR. We thus apply a small baryonic-mass correction ($1/f_{\star} = 1.25$ or 0.1 dex) to Equation (4) to obtain the coefficients of the CO baryonic TFR:

$$\begin{aligned} a &= 10.61 \pm 0.04 \\ b &= 3.3 \pm 0.3 \\ c &= 2.58. \end{aligned} \quad (5)$$

The advantage of a baryonic TFR is that the same locally calibrated relation may still be valid at higher redshifts, because neither the dynamical equilibrium physics nor the baryonic-to-dark-matter mass ratio of halos is expected to strongly evolve with redshift (McGaugh 2012). In contrast, the *stellar-mass* TFR evolves with redshift (Cresci et al. 2009; Miller et al. 2011, 2012), likely because of the increase in gas fraction with redshift.

To utilize the TFR for the mass estimation of individual galaxies, one must correct the line width for the inclination angle of the disk, which is not always available especially at high redshifts due to limited spatial resolution. Therefore, we correct the inclination angles statistically, by considering the galaxies in each population as randomly oriented disks. We can determine the average f'_{mol} of the population by matching the distribution of observables with the expected probability density function (PDF).

We begin by expressing the relations between the observed properties (w , L'_{CO}) and their true values as

$$\begin{aligned} \log w &= \log(w_{\text{true}}) + \epsilon_w \\ \log L'_{\text{CO}} &= \log L'_{\text{CO,true}} + \epsilon_L. \end{aligned} \quad (6)$$

Here, $w_{\text{true}} \equiv W_{\text{true}} \sin i$ is the true line FWHM. The random variables (ϵ_w and ϵ_L) represent the fractional measurement

errors:

$$\begin{aligned} \epsilon_w &\equiv \log \frac{w}{w_{\text{true}}} \simeq \frac{1}{\ln 10} \frac{w - w_{\text{true}}}{w_{\text{true}}} \\ \epsilon_L &\equiv \log \frac{L'_{\text{CO}}}{L'_{\text{CO,true}}} \simeq \frac{1}{\ln 10} \frac{L'_{\text{CO}} - L'_{\text{CO,true}}}{L'_{\text{CO,true}}}. \end{aligned} \quad (7)$$

Next, we rewrite the α_{CO} -normalized molecular gas fraction f'_{mol} defined in Equation (2) using the relations in Equation (6) and the TFR in Equation (3) as

$$\begin{aligned} \log f'_{\text{mol}} &= \log L'_{\text{CO,true}} - \log M_{\text{bary,true}} \\ &= (\log L'_{\text{CO}} - \epsilon_L) \\ &\quad - [a + b(\log w - \log(\sin i) - \epsilon_w - c)]. \end{aligned} \quad (8)$$

Finally, we can rearrange the above equation and get

$$\begin{aligned} \log L'_{\text{CO}} - [a + b(\log w - c)] \\ &= \log f'_{\text{mol}} + \epsilon_L - b\epsilon_w - b \log(\sin i) \\ &\equiv \log f'_{\text{mol}} + X, \end{aligned} \quad (9)$$

in which the left side is a combined observable that can be determined from the CO measurement pair (w , L'_{CO}), while the right side is the sum between $\log f'_{\text{mol}}$ and a linear combination of three random variables, expressed as $X \equiv \epsilon_L - b\epsilon_w - b \log(\sin i)$. If the PDFs of these random variables are known, one can estimate $\log f'_{\text{mol}}$ by matching the expected PDF of $\log f'_{\text{mol}} + X$ to the observed distribution of $\log L'_{\text{CO}} - [a + b(\log w - c)]$ for a galaxy population.

As a linear combination of three independent random variables, the PDF of X is the convolution of their individual PDFs:

$$f_X(x) = f_{\epsilon_L}(x) * f_{-b\epsilon_w}(x) * f_{-b \log(\sin i)}(x). \quad (10)$$

Because ϵ_w and ϵ_L represent fractional measurement errors (Equation (7)), we can assume that they are drawn from two Gaussian distributions with dispersions of σ_w and σ_L , respectively. Their convolution is still a Gaussian, and we have the PDF of $(\epsilon_L - b\epsilon_w)$:

$$f_{\epsilon_L - b\epsilon_w}(x) = \frac{1}{\sigma\sqrt{2\pi}} e^{-x^2/2\sigma^2} \quad (11)$$

$$\sigma^2 = b^2\sigma_w^2 + \sigma_L^2. \quad (12)$$

On the other hand, given the PDF of the inclination angle i for random orientations, $f_i(x) = \sin x$ for $0 \leq x \leq \pi/2$, we derive the PDF of $-b \log(\sin i)$:

$$f_{-b \log(\sin i)}(x) = \begin{cases} \frac{\ln 10}{b} \frac{10^{-2x/b}}{\sqrt{1 - 10^{-2x/b}}} & x \geq 0 \\ 0 & x < 0 \end{cases} \quad (13)$$

Its convolution with Equation (11) gives the expected PDF of X :

$$f_X(x) = \frac{\ln 10}{b} \int_0^{\infty} \frac{10^{-2t/b}}{\sqrt{1 - 10^{-2t/b}}} \frac{1}{\sigma\sqrt{2\pi}} e^{-(x-t)^2/2\sigma^2} dt, \quad (14)$$

which peaks near zero. As a result, the PDF of $\log f'_{\text{mol}} + X$ peaks near $\log f'_{\text{mol}}$.

To obtain the model parameters (f'_{mol} , σ) that best describe the data, we write down the likelihood function of the observed data set $\{w_k, L'_{\text{CO},k}\}$ given a model described by f'_{mol} and σ as

$$\mathcal{L}(f'_{\text{mol}}, \sigma) \equiv p(\{w_k, L'_{\text{CO},k}\} | f'_{\text{mol}}, \sigma) = \prod_k f_X(x_k), \quad (15)$$

where f_X is from Equation (14) and x_k is calculated for the k th galaxy in the population

$$x_k = \log L'_{\text{CO},k} - [a + b(\log w_k - c)] - \log f'_{\text{mol}}. \quad (16)$$

This likelihood function is maximized when the model parameters best describe the observed data set. Using Bayes' Theorem, the posterior PDF of the model given the data, $p(f'_{\text{mol}}, \sigma | \{w_k, L'_{\text{CO},k}\})$, is the product of the likelihood function and the model prior $p(f'_{\text{mol}}, \sigma)$:

$$p(f'_{\text{mol}}, \sigma | \{w_k, L'_{\text{CO},k}\}) \propto \mathcal{L}(f'_{\text{mol}}, \sigma) p(f'_{\text{mol}}, \sigma). \quad (17)$$

To sample the posterior PDFs and quantify the best-fit values of (f'_{mol} , σ) and their uncertainties, we use the Affine Invariant Markov chain Monte Carlo (MCMC) Ensemble sampler implemented in Python code `emcee`³ (Foreman-Mackey et al. 2013). We assume bounded “flat” priors for both $\log f'_{\text{mol}}$ and σ : $-10 \leq \log f'_{\text{mol}} \leq 10$ and $0 \leq \sigma \leq 10$.

4. Results

In Table 1, we report the the median values of the marginalized posterior distributions from the MCMC chains as the best-fit parameters and the 15.8% and 84.1% values as the 1σ confidence intervals. To illustrate how well our models describe the data, in Figure 2 we compare the model PDFs using the best-fit parameters from `emcee` and the observed distribution of $\log L'_{\text{CO}} - [a + b(\log w - c)]$ for each galaxy population. For all six populations, the model PDFs fit the histograms quite well, validating the `emcee` results.

4.1. The Evolution of Molecular Gas Fraction

In the previous section, we have shown that the CO measurements alone can provide an estimate of the mean molecular gas fraction for a galaxy population, given a baryonic TFR and a CO–H₂ conversion factor. The histograms and best-fit models in Figure 2 clearly show a redshift evolution of the α_{CO} -normalized molecular gas fraction (f'_{mol}), as highlighted by the offsets in their peaks. To better illustrate this redshift evolution, we plot f_{mol} as a function of redshift in Figure 3 for the six galaxy populations compiled in Table 1. To convert f'_{mol} to f_{mol} , we have applied a fiducial α_{CO} value of $1 M_{\odot}/L_I$ for all populations in both Figure 3 and in Table 1. The redshift evolution of the gas fraction is evident, and it roughly follows a power law $f_{\text{mol}} \propto (1+z)^{\beta}$ with $\beta \sim 2$ between $0 < z < 3$.

As a consistency check, we compare our results with the observed redshift evolution of the star-forming main sequence. The molecular gas fraction can be inferred from the normalization of the star-forming main sequence (i.e., the specific SFR, $\text{sSFR} = \text{SFR}/M_{\star}$) and the Kennicutt–Schmidt star formation relation ($\text{SFR} = M_{\text{mol}}/\tau$, where τ is the gas

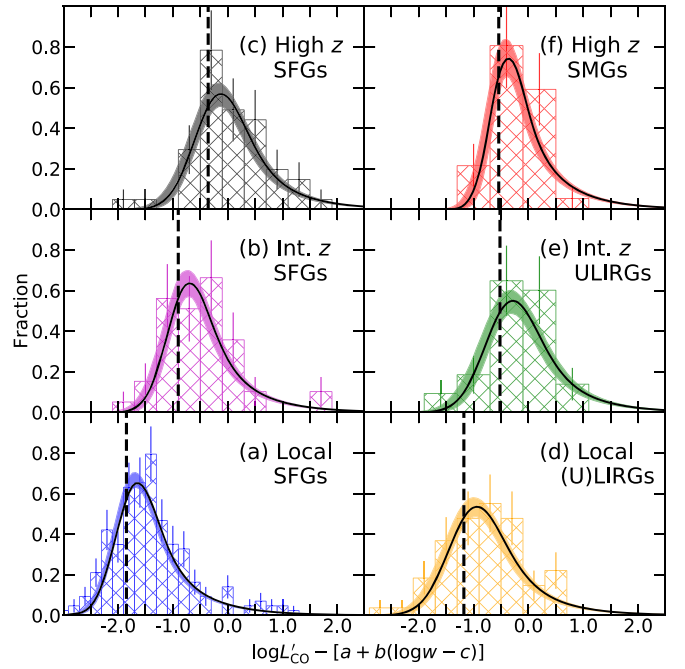


Figure 2. CO data vs. best-fit model for normal star-forming populations (left panels) and starburst populations (right panels). The histograms show the distributions of the vertical offsets of the data points from the left-most dashed line in Figure 1, which is calculated as $\log L'_{\text{CO}} - [a + b(\log w - c)]$ (i.e., the left side of Equation (9)). The black solid curves show the PDF of $\log f'_{\text{mol}} + X$ (i.e., the right side of Equation (9)) using the best-fit parameters from the MCMC chains. The color-shaded regions around each curve show the 1σ confidence intervals of the PDFs, and the dashed vertical lines indicate the best-fit $\log f'_{\text{mol}}$. To compare with the PDFs, the histograms are plotted in units of fraction per dex for 0.2–0.6 dex bins. The error bars indicate Poisson noise. These histograms are shown for illustration only and are not used in the inference of best-fit parameters.

depletion timescale) because

$$f_{\text{mol}} \simeq \frac{M_{\text{mol}}}{M_{\text{mol}} + M_{\star}} = \frac{\text{sSFR} \cdot \tau}{1 + \text{sSFR} \cdot \tau}. \quad (18)$$

For main-sequence SFGs, it is appropriate to use a gas depletion timescale of $\tau \sim 0.7$ Gyr (e.g., Tacconi et al. 2013; Saintonge et al. 2017).⁴ The observed sSFR of main-sequence SFGs depends strongly on redshift and mildly on stellar mass, and the best-fit polynomial function is (see references in Tacconi et al. 2013, for the original data)

$$\text{sSFR} = 0.68 \text{ Gyr}^{-1} \left(\frac{M_{\star}}{6.6 \times 10^{10} M_{\odot}} \right)^{-0.35} \left(\frac{1+z}{2.2} \right)^{2.8}. \quad (19)$$

Using the above two relations, we can infer f_{mol} at any given redshift and stellar mass. The curves and shaded areas in Figure 3 show the inferred evolution of f_{mol} at fixed stellar masses of $M_{\star} = 10^9, 10^{10}, 10^{11} M_{\odot}$. Without making any adjustments, our results closely follow the trend inferred from the observed evolution of the main sequence in Figure 3. Almost all of the data points follow the curve for a stellar

⁴ Note that Tacconi et al. (2013) inferred a $\sim 2\times$ longer gas depletion timescale ($\tau = 1.5$ Gyr at $z \sim 0$) from COLD GASS because the SFR at $M_{\star} \sim 10^{10.5} M_{\odot}$ used in Saintonge et al. (2017) is $\sim 2\times$ lower than the best-fit SFR from Equation (19). For consistency, we adopt $\tau = 0.7$ Gyr at all redshifts.

³ <http://dfm.io/emcee>

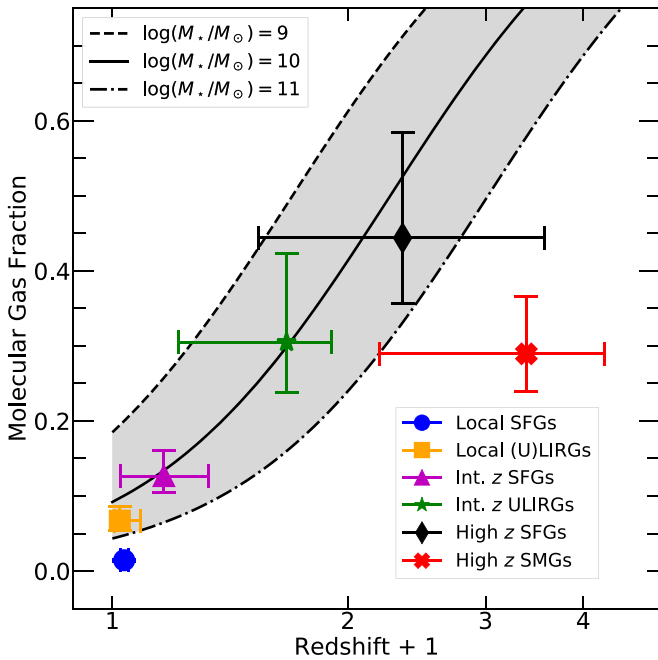


Figure 3. Redshift evolution of the molecular gas fraction. The plotted f_{mol} values and their uncertainties are calculated from $\log f'_{\text{mol}}$ assuming $\alpha_{\text{CO}} = 1.0 M_{\odot}/L_I$ for all populations. Data points are plotted at the median redshift of each population with horizontal error bars representing the redshift range. For comparison, the dashed, solid, and dashed-dotted curves show the inferred f_{mol} evolution for stellar masses of 10^9 , 10^{10} , and $10^{11} M_{\odot}$, respectively, based on the observed evolution of the star-forming main sequence and a Kennicutt–Schmidt relation (Equations (18) and (19)).

masses between $10^{10} < M_{\star} < 10^{11} M_{\odot}$, except for the local SFGs and the high- z SMGs.

For the local SFGs, the plotted f_{mol} lies significantly below the shaded area because a higher Galactic-like CO–H₂ conversion factor is more appropriate for these galaxies. Using the Milky Way value of $\alpha_{\text{CO}} = 4.3 M_{\odot}/L_I$, f_{mol} increases from 1.4% to 6.0%, approaching the shaded area in Figure 3 and becoming consistent with that of local (U)LIRGs ($6.7^{+1.3}_{-1.7}\%$). By design, this is in perfect agreement with the mean molecular gas fraction of $f_{\text{mol}} \simeq 6\%$ for the same COLD GASS sample, based on a direct calculation using their stellar masses, HI masses, and molecular masses ($M_{\text{mol}}/(M_{\star} + M_{\text{HI}} + M_{\text{mol}})$). But on the other hand, if we assume that local SFGs and local (U)LIRGs should have similar molecular fractions, then the best-fit f'_{mol} values would indicate that the former should have a 4.8 ± 1.2 times greater α_{CO} value than the latter. This is consistent with the findings from previous α_{CO} studies of local (U)LIRGs (e.g., Downes & Solomon 1998; Papadopoulos et al. 2012).

Our model shows that the SMGs have a mean molecular gas fraction of $f_{\text{mol}} = 28^{+5}_{-7}\%$ for $\alpha_{\text{CO}} = 1.0 M_{\odot}/L_I$ at $\bar{z} \sim 2.5$. Similar to local SFGs, their data point lies significantly below the solid curve in Figure 3. But for the SMGs, the adopted starburst-like CO–H₂ conversion factor is supported by other observations (e.g., Magdis et al. 2011; Hodge et al. 2012; Magnelli et al. 2012; Xue et al. 2018). There are two possible ways to explain this result. First, the SMGs contain a large fraction of mergers that are spatially unresolved in the CO observations (e.g., Engel et al. 2010; Fu et al. 2012, 2013). The relative velocities between merging components increase the line widths and thus decrease the molecular gas fraction inferred from the TFR. Second, the SMGs may have stellar

masses exceeding $10^{11} M_{\odot}$, which is higher than the stellar mass of high- z SFGs from the PHIBSS survey ($M_{\star} \sim 10^{10.5} M_{\odot}$; Tacconi et al. 2013). The mean stellar mass of SMGs is still a matter of debate, with estimates between $\sim 5 \times 10^{10} M_{\odot}$ (Hainline et al. 2011) and $\sim 3 \times 10^{11} M_{\odot}$ (e.g., Michałowski et al. 2010, 2012). Our current estimate is more consistent with the higher estimate.

Lastly, if we were to adopt the higher Galactic-like CO–H₂ conversion factor on the high- z SFGs, f_{mol} would exceed 100%, which is unphysical. We thus obtain an upper limit on the CO–H₂ conversion factor of $\alpha_{\text{CO,SFG}} < 2.3^{+0.9}_{-0.4} M_{\odot}/L_I$ for SFGs at $\bar{z} \sim 1.5$. Similarly, for SMGs, the upper limit is at $\alpha_{\text{CO,SB}} < 3.5^{+1.1}_{-0.6} M_{\odot}/L_I$.

4.2. Systematic Uncertainties from the TFR

In the above analysis, we have ignored the uncertainties of the TFR itself, which include uncertainties of the zero-point mass (parameter a), the slope (parameter b), and the intrinsic scattering (σ_{int}).

Tiley et al. (2016) quoted 1σ uncertainties of 0.04 dex in a and 0.3 in b (which is also 0.04 dex because $b = 3.3$). We examine the systematic uncertainties of the best-fit f'_{mol} values by varying the coefficients of the TFR and repeating the analysis. We find that the above uncertainties of the a and b coefficients translate to systematic uncertainties of f'_{mol} around 0.04, 0.06, and 0.1 dex for the local, intermediate- z , and high- z samples, respectively. In all cases, the systematic uncertainty is comparable to or smaller than the statistical errors from the MCMC chains.

The measured TFR zero-point mass and the slope are also known to vary among different studies, depending on their choices of the kinematics and the mass tracers. For example, the TFRs based on the asymptotic rotation velocity or the velocity along the flat part of a resolved rotation curve typically exhibit steeper slope ($b \sim 4$; e.g., Miller et al. 2011; McGaugh & Schombert 2015; Papastergis et al. 2016) than those based on line width (e.g., McGaugh 2012; Tiley et al. 2016). Additionally, the TFRs using HI, H α , [O II] may differ from those using CO, because the kinematics tracers could sample different spatial scales in a galaxy. We chose the CO TFR from Tiley et al. (2016) to minimize the impact from these systematics because it uses the width of a low- J CO line, similar to the application in this study. Nevertheless, because varying the TFR coefficients would change the estimated f'_{mol} values of all galaxy populations along the same direction, the observed redshift evolution of f'_{mol} is unchanged.

At a given line width, an intrinsic scatter of $\sigma_{\text{int}} = 0.1\text{--}0.2$ dex in mass is expected in the baryonic TFR, due to the variations in the mass concentration relation of dark-matter halos and the baryonic-to-halo mass ratio (e.g., Dutton 2012). Because the intrinsic scatter of the TFR affects the observables in the same way as measurement errors, the dispersion parameter σ of our model should include the contribution from σ_{int} ; specifically, $\sigma^2 = b^2\sigma_w^2 + \sigma_L^2 + \sigma_{\text{int}}^2$. But the observational uncertainties are not qualified accurately enough to separate the measurement errors and the intrinsic scatter in σ . The expected intrinsic scatter of 0.1–0.2 dex is significantly smaller than what we measured from the data ($\sigma \simeq 0.4\text{--}0.6$ dex; see Table 1), which appear to be dominated by the measurement error of line width ($b \sigma_w \sim 0.35$ dex for a typical error of 25%).

5. Summary and Future Prospects

In summary, we have developed a new method to infer the mean molecular gas fraction of a galaxy population. This method requires only spatially integrated low- J CO observations and corrects the inclination effects statistically. This is possible because (1) the CO line luminosity traces with the molecular gas mass through a CO–H₂ conversion factor; (2) the CO line width, once corrected for the disk inclination angle, provides the total baryonic mass, M_{bary} , given a baryonic CO TFR; and (3) the ratio of the two, $L'_{\text{CO}}/M_{\text{bary}}$, is the α_{CO} -normalized molecular gas fraction, defined as $f'_{\text{mol}} \equiv f_{\text{mol}}/\alpha_{\text{CO}}$. We use the expected PDF of the inclination angle from randomly oriented disks to correct the inclination effect statistically. The model also accounts for the measurement errors and the intrinsic dispersion of the TFR in a dispersion parameter σ . From the literature, we have compiled CO measurements for three populations of normal SFGs and three populations of starburst galaxies with redshifts stretching between $0.01 < z < 3.26$. We use Bayesian inference and the MCMC sampler `emcee` to derive the joint and marginalized PDFs for f'_{mol} and σ from the CO data of each populations. Our main findings are as follows.

1. The molecular gas fraction increases rapidly with redshift for both normal SFGs and starbursts. The evolution trend is consistent with that indirectly inferred from the observed evolution of the star-forming main sequence and a Kennicutt–Schmidt relation;
2. By comparing the inferred f'_{mol} values for the local SFGs and local (U)LIRGs, we find that the two populations would have similar molecular gas fractions only if a $\sim 5\times$ higher α_{CO} conversion factor is used for the former population, which is consistent with previous α_{CO} studies of local galaxies;
3. At higher redshifts ($z > 1$), our results suggest a lower starburst-like α_{CO} is applicable for both main-sequence galaxies and starbursts. In fact, the upper limit of molecular gas fraction at 100% translates to upper limits of α_{CO} for these populations: $\alpha_{\text{CO,SFG}} < 2.3^{+0.9}_{-0.4} M_{\odot}/L_I$ and $\alpha_{\text{CO,SB}} < 3.5^{+1.1}_{-0.6} M_{\odot}/L_I$ for high- z SFGs and starbursts, respectively;
4. The molecular gas fraction of SMGs is relatively low compared to that of coeval main-sequence galaxies, indicating a significant fraction of unresolved mergers and/or an average stellar mass exceeding $10^{11} M_{\odot}$.

Clearly, our results hinge upon the assumption that the baryonic CO TFR does not evolve with redshift. Galaxy formation models suggest weak evolution of the baryonic TFR utilizing the maximum circular velocity (v_{max}), because individual galaxies evolve along such scaling relations (e.g., Dutton et al. 2011). To extend the theoretical expectation to the CO TFR we adopted, we have implicitly assumed a nearly constant ratio between v_{max} and the CO FWHM. This assumption can be tested with future spatially resolved measurements of rotation curves in a large sample of galaxies across a wide redshift range.

While our choice of the CO lines was motivated by their availability in the literature, they are also favored for several other reasons. First, they allow us to calibrate the TFR with local galaxies and apply it at higher redshifts with the same kinematic tracer (CO FWHM), thereby easing the concern of the systematic biases introduced by different kinematic tracers

(see Bradford et al. 2016). Second, we have restricted the sample to galaxies with low- J CO measurements, which are expected to have a larger spatial extent than high- J CO emission. In both local and high- z galaxies, we expect that a substantial fraction of the low- J CO emission reaches the flat part of the rotation curve (e.g., Downes & Solomon 1998; Hodge et al. 2012; Xue et al. 2018; Pereira-Santaella et al. 2018). Lastly, given the higher gas fraction and larger molecular-to-atomic ratio at high redshifts (e.g., Lagos et al. 2011), we would expect that the low- J CO lines are even more effective at tracing global kinematics at high redshifts than in nearby galaxies.

The likelihood method presented here can also be used to measure TFRs without knowing the inclination angles of individual galaxies, which is particularly useful for high- z galaxies. Similar to the “inclination-free” maximum likelihood estimation method of Obreschkow & Meyer (2013), a galaxy sample only needs to have measurements of the mass (either stellar or baryonic mass) and the line width to measure the TFR. This Bayesian-based analysis can yield reliable measurements of the TFR if the sample contains enough objects (ideally $N > 50$) and has roughly uniform measurement errors.

Future studies of the molecular gas fraction will certainly benefit from more and better CO data from large surveys. The Atacama Spectroscopic Survey (Walter et al. 2016) is a good start toward a wide-field blind CO survey, while the next generation Very Large Array (VLA) will further probe *unlensed* CO(1 \rightarrow 0) transitions at $z > 1.5$ (Decarli et al. 2018; Emonts et al. 2018). In addition, one can apply the same method on the original TFR tracer, the HI 21 cm line, to study the atomic gas fraction evolution. Such a study will be viable when HI detections of large samples of galaxies become available up to $z \simeq 0.6$ with the VLA (e.g., Fernández et al. 2016) and up to $z \simeq 1.4$ with the Square Kilometer Array (e.g., Booth et al. 2009; Allison et al. 2015).

We thank the anonymous referee for helpful comments and acknowledge support from the National Science Foundation (NSF) grant AST-1614326.

ORCID iDs

Jacob W. Isbell  <https://orcid.org/0000-0002-1272-6322>

Rui Xue  <https://orcid.org/0000-0001-7689-9305>

Hai Fu  <https://orcid.org/0000-0001-9608-6395>

References

- Allison, J. R., Sadler, E. M., Moss, V. A., et al. 2015, *MNRAS*, **453**, 1249
 Armus, L., Mazzarella, J. M., Evans, A. S., et al. 2009, *PASP*, **121**, 559
 Bigiel, F., Leroy, A., Walter, F., et al. 2008, *AJ*, **136**, 2846
 Blitz, L. 1993, in *Protostars and Planets III*, ed. E. H. Levy & J. I. Lunine (Tucson, AZ: Univ. Arizona Press), 125
 Bolatto, A. D., Wolfire, M., & Leroy, A. K. 2013, *ARA&A*, **51**, 207
 Booth, R. S., de Blok, W. J. G., Jonas, J. L., & Fanaroff, B. 2009, arXiv:0910.2935
 Bothwell, M. S., Maiolino, R., Kennicutt, R., et al. 2013, *MNRAS*, **433**, 1425
 Bothwell, M. S., Smail, I., Chapman, S. C., et al. 2013, *MNRAS*, **429**, 3047
 Bouché, N., Dekel, A., Genzel, R., et al. 2010, *ApJ*, **718**, 1001
 Bradford, J. D., Geha, M. C., & van den Bosch, F. C. 2016, *ApJ*, **832**, 11
 Bussmann, R. S., Pérez-Fournon, I., Amber, S., et al. 2013, *ApJ*, **779**, 25
 Carilli, C. L., & Walter, F. 2013, *ARA&A*, **51**, 105
 Catinella, B., Saintonge, A., Janowiecki, S., et al. 2018, *MNRAS*, **476**, 875
 Chiu, K., Bamford, S. P., & Bunker, A. 2007, *MNRAS*, **377**, 806
 Combes, F., García-Burillo, S., Braine, J., et al. 2011, *A&A*, **528**, A124
 Combes, F., García-Burillo, S., Braine, J., et al. 2013, *A&A*, **550**, A41
 Cresci, G., Hicks, E. K. S., Genzel, R., et al. 2009, *ApJ*, **697**, 115

- Davis, T. A., Bureau, M., Young, L. M., et al. 2011, *MNRAS*, 414, 968
- Decarli, R., Carilli, C., Casey, C., et al. 2018, arXiv:1810.07546
- Downes, D., & Solomon, P. M. 1998, *ApJ*, 507, 615
- Dutton, A. A. 2012, *MNRAS*, 424, 3123
- Dutton, A. A., van den Bosch, F. C., Faber, S. M., et al. 2011, *MNRAS*, 410, 1660
- Emonts, B., Carilli, C., Narayanan, D., Lehnert, M., & Nyland, K. 2018, arXiv:1810.06770
- Engel, H., Tacconi, L. J., Davies, R. I., et al. 2010, *ApJ*, 724, 233
- Fernández, X., Gim, H. B., van Gorkom, J. H., et al. 2016, *ApJL*, 824, L1
- Foreman-Mackey, D., Hogg, D. W., Lang, D., & Goodman, J. 2013, *PASP*, 125, 306
- Fu, H., Cooray, A., Feruglio, C., et al. 2013, *Natur*, 498, 338
- Fu, H., Jullo, E., Cooray, A., et al. 2012, *ApJ*, 753, 134
- Greve, T. R., Leonidaki, I., Xilouris, E. M., et al. 2014, *ApJ*, 794, 142
- Hainline, L. J., Blain, A. W., Smail, I., et al. 2011, *ApJ*, 740, 96
- Harris, A. I., Baker, A. J., Frayer, D. T., et al. 2012, *ApJ*, 752, 152
- Haynes, M. P., Giovanelli, R., Kent, B. R., et al. 2018, arXiv:1805.11499
- Ho, L. C. 2007, *ApJ*, 669, 821
- Hodge, J. A., Carilli, C. L., Walter, F., et al. 2012, *ApJ*, 760, 11
- Iverson, R. J., Papadopoulos, P. P., Smail, I., et al. 2011, *MNRAS*, 412, 1913
- Kennicutt, R. C., & Evans, N. J. 2012, *ARA&A*, 50, 531
- Lagos, C. D. P., Baugh, C. M., Lacey, C. G., et al. 2011, *MNRAS*, 418, 1649
- Magdis, G. E., Daddi, E., Elbaz, D., et al. 2011, *ApJL*, 740, L15
- Magdis, G. E., Rigopoulou, D., Hopwood, R., et al. 2014, *ApJ*, 796, 63
- Magnelli, B., Saintonge, A., Lutz, D., et al. 2012, *A&A*, 548, 22
- McGaugh, S. S. 2012, *AJ*, 143, 40
- McGaugh, S. S., & Schombert, J. M. 2015, *ApJ*, 802, 18
- McKee, C. F., & Ostriker, E. C. 2007, *ARA&A*, 45, 565
- Michałowski, M., Hjorth, J., & Watson, D. 2010, *A&A*, 514, A67
- Michałowski, M. J., Dunlop, J. S., Cirasuolo, M., et al. 2012, *A&A*, 541, 85
- Miller, S. H., Bundy, K., Sullivan, M., Ellis, R. S., & Treu, T. 2011, *ApJ*, 741, 115
- Miller, S. H., Ellis, R. S., Sullivan, M., et al. 2012, *ApJ*, 753, 74
- Noeske, K. G., Weiner, B. J., Faber, S. M., et al. 2007, *ApJL*, 660, L43
- Obreschkow, D., & Meyer, M. 2013, *ApJ*, 777, 140
- Obreschkow, D., & Rawlings, S. 2009, *ApJL*, 696, L129
- Papadopoulos, P. P., van der Werf, P., Xilouris, E., Isaak, K. G., & Gao, Y. 2012, *ApJ*, 751, 10
- Papastergis, E., Adams, E. A. K., & van der Hulst, J. M. 2016, *A&A*, 593, A39
- Pereira-Santaella, M., Colina, L., García-Burillo, S., et al. 2018, *A&A*, 616, A171
- Saintonge, A., Catinella, B., Tacconi, L. J., et al. 2017, *ApJS*, 233, 22
- Saintonge, A., Kauffmann, G., Kramer, C., et al. 2011, *MNRAS*, 415, 32
- Saito, T., Iono, D., Xu, C. K., et al. 2017, *ApJ*, 835, 174
- Schoniger, F., & Sofue, Y. 1994, *A&A*, 283, 21
- Solomon, P. M., Downes, D., Radford, S. J. E., & Barrett, J. W. 1997, *ApJ*, 478, 144
- Sorce, J. G., Courtois, H. M., Tully, R. B., et al. 2013, *ApJ*, 765, 94
- Springob, C. M., Haynes, M. P., Giovanelli, R., & Kent, B. R. 2005, *ApJS*, 160, 149
- Tacconi, L. J., Genzel, R., Neri, R., et al. 2010, *Natur*, 463, 781
- Tacconi, L. J., Genzel, R., Saintonge, A., et al. 2018, *ApJ*, 853, 179
- Tacconi, L. J., Neri, R., Genzel, R., et al. 2013, *ApJ*, 768, 74
- Tiley, A. L., Bureau, M., Saintonge, A., et al. 2016, *MNRAS*, 461, 3494
- Topal, S., Bureau, M., Tiley, A. L., Davis, T. A., & Torii, K. 2018, *MNRAS*, 479, 3319
- Tully, R. B., & Courtois, H. M. 2012, *ApJ*, 749, 78
- Tully, R. B., & Fisher, J. R. 1977, *A&A*, 54, 661
- Turner, O. J., Harrison, C. M., Cirasuolo, M., et al. 2017, arXiv:1711.03604
- Übler, H., Förster Schreiber, N. M., Genzel, R., et al. 2017, *ApJ*, 842, 121
- Villanueva, V., Ibar, E., Hughes, T. M., et al. 2017, *MNRAS*, 470, 3775
- Walter, F., Decarli, R., Aravena, M., et al. 2016, *ApJ*, 833, 67
- Wong, T., & Blitz, L. 2002, *ApJ*, 569, 157
- Xue, R., Fu, H., Isbell, J., et al. 2018, *ApJL*, 864, L11
- Yamashita, T., Komugi, S., Matsuhara, H., et al. 2017, *ApJ*, 844, 96
- Zaritsky, D., Courtois, H., Muñoz-Mateos, J.-C., et al. 2014, *AJ*, 147, 134